PAPER

Check for updates

Theoretical design of double anti-perovskite Na$_6$SOI$_2$ as a super-fast ion conductor for solid Na$^+$ ion batteries†

Yuran Yu, [ID] [ab] Zhuo Wang [ID] *[ab] and Guosheng Shao [ID] *[ab]

Development of non-flammable solid electrolytes is necessary for sodium ion batteries, so that a sustainable battery technology can be extensively exploited for large scale energy storage when safety is of utmost importance. Here in this work, we have carried out extensive fundamental modelling, in search of solid electrolytes with superb ionic conductivity for Na$^+$. A new class of materials is identified, based on a cubic double anti-perovskite phase of Na$_6$SOI$_2$. Through moderate off-stoichiometric composition setting to tune the alloy chemistry, *e.g.* Na$_{25}$S$_5$O$_4$I$_7$, superfast ionic conductivity is predicted with an activation energy as low as 0.16 eV for Na$^+$, and remarkable ionic conductivity of 10.36 mS cm^{-1} at room temperature and even 1.79 mS cm^{-1} at −50 °C. Besides, the new solid electrolyte is electrochemically compatible with Na anodes and has a wide energy gap to prevent conduction of electrons.

Introduction

Li-ion rechargeable batteries (LIBs) have been extensively exploited for energy storage, particularly in electric vehicles and portable electronic devices, wherein high energy density is demanded.[1–3] Currently, great efforts are directed towards developing solid-state electrolytes (SSEs), in order to address safety concerns due to the flammability of organic liquid electrolytes used in commercial LIBs.[4] Another concern about LIBs lies in the limited lithium resources, which imposes a potential threat to sustainable application of LIBs to meet the ever increasing demand for energy storage.[5] Such a concern about resource sustainability is behind another current drive to develop alternative metal ion batteries based on more abundant metal resources, such as sodium (Na$^+$),[6] potassium (K$^+$),[7] magnesium (Mg^{2+})[8,9] and zinc (Zn^{2+}).[10] Among such alternative metal ion batteries, sodium-ion batteries (SIBs) are most attractive, because of the extremely large resources of sodium and its much lower cost than lithium.[2] Ever increasing efforts have therefore been made to develop SIBs, which are largely considered for static energy storage due to their lower energy density than LIBs.[6,11]

As sodium is next to lithium in the alkali group of metals, the extensive knowledge from LIBs has naturally been a source of inspiration for developing SIBs, so that all aspects of LIB research have been extended to SIBs. Safety concerns about organic electrolytes have thus been extended to developing SSEs for SIBs, largely mirroring the SSE work for LIBs. However, there are also distinct differences between the two ions. The radius of the sodium ion (1.02 Å) is about twice that of the lithium ion (0.76 Å), its atomic mass is much heavier than that of lithium, and the standard electrode potential of sodium [−2.71 V *vs.* the standard hydrogen electrode (SHE)] is higher than that of lithium [−3.05 V *vs.* SHE].[6] This makes straightforward replication of LIB materials for SIB applications problematic.[12]

Similar to SSEs for LIBs,[13–15] an ideal SSE for SIBs is expected to meet the following criteria: (a) having an excellent Na$^+$ ion conductivity greater than 1 mS cm^{-1} (current technical requirement for liquid organic electrolytes), (b) having low electrical conductivity to avoid self-discharging in batteries, (c) being stable over the wide temperature range from −100 to 300 °C, (d) being electrochemically compatible with sodium anodes,[16] so as to make the best use of the extremely high energy density of Na anodes (1.16 A h g^{-1}) at a low electrode potential (−2.71 V),[6] and (e) being light, cheap, and environmentally friendly.

The milestone discovery of Li$_{10}$GeP$_2$S$_{12}$ (LGPS)[17,18] showed for the first time that a SSE could rival liquid organic electrolytes with an even superior alkali ion conductivity, up to 10 mS cm^{-1} at room temperature. Straightforward substitution of Li with Na was, however, not as successful, even though the Na$_{10}$MP$_2$S$_{12}$ (M = Ge, Si, Sn), or NGPS, compound could assume the same LGPS-type space group (*P*4$_2$/*nmc*). While first-principles calculations

^{a}State Center for International Cooperation on Designer Low-carbon & Environmental Materials (CDLCEM), Zhengzhou University, 100 Kexue Avenue, Zhengzhou 450001, China. E-mail: gsshao@zzu.edu.cn

^{b}Zhengzhou Materials Genome Institute (ZMGI), Zhongyuanzhigu, Building 2, Xingyang 450100, China. E-mail: wangzh@zzu.edu.cn

This journal is © The Royal Society of Chemistry 2018

J. Mater. Chem. A, 2018, **6**, 19843–19852 | 19843

showed the same one-dimensional fast Na^+ diffusion channel along the c-axis as that in LGPS,[19] the activation barrier in the stoichiometric $Na_{10}SnP_2S_{12}$ compound[20] was predicted to be 0.317 eV ($vs.$ 0.25 eV for LGPS). Experimental investigation showed that the activation barrier for Na transport was slightly higher than the theoretical value, being 0.356 eV, and the room temperature ionic conductivity of Na was only 0.4 mS cm^{-1}. Afterward, through stoichiometric offsetting with excess Na, $Na_{11}Sn_2PS_{12}$ with a tetragonal space group $I4_1/acd$ was synthesized.[19] Both the activation barrier and ionic conductivity were significantly promoted. The overall activation energy for Na-ion transport was determined to be 0.25 eV and the ionic conductivity reached 1.4 mS cm^{-1} at room temperature. These have been the best properties for this class of SSE materials. However, due to the marginal room temperature conductivity, such a SSE can only serve above 17 °C, which is inadequate for practical applications. Also, being similar to LGPS with lithium, this electrolyte was also found to be electrochemically incompatible with Na anodes.[19] The SSE stability window $vs.$ Na was only 0.57 V (from 1.25 to 1.82 V), which cannot prevent undesirable interphase formation below 1.25 V with the Na anode or above 1.82 V with the cathode.[20]

Some alternative SSE candidates for SIBs were developed to achieve better electrochemical stability $vs.$ Na anodes than $Na_{11}Sn_2PS_{12}$. For example, a sulphide glass–ceramic electrolyte Na_3PS_4 (ref. 21 and 22) had a moderate activation barrier of 0.28 eV, though Na^+ conductivity at room temperature was only 0.2 mS cm^{-1}. No improvement was achieved through Se substitution of S, such that a Na_3PSe_4 compound in the same family had an even lower ionic conductivity of 0.1 mS cm^{-1}.[23,24] Substitution of P sites by Sb resulted in a tetragonal Na_3SbS_4 (ref. 25 and 26) compound, which possessed two-dimensional (2D) channels for sodium ion diffusion. However, the total ionic conductivity was rather poor, due to the rather high resistance around 30 kΩ attributed to boundary charge transfer.[25] Efforts in exploiting oxides as SSEs for SIBs were not successful due to their rather poor ionic conductivity, even though they could be of good structural stability. For example, $Na_{1+x}Zr_2Si_xP_{3-x}O_{12}$ (NZSP, $0 \leq x \leq 3$)[27] and $Na_{3-x}V_{2-x}Zr_x(PO_4)_3$ (NVP)[28] had best reported ionic conductivities of 0.1 mS cm^{-1} and 1.8×10^{-4} mS cm^{-1} at room temperature respectively. Overall, in spite of significant efforts in developing SSEs for solid SIBs, achievements so far are still short of practical requirements in terms of both ionic conductivity below room temperature and electrochemical compatibility with Na anodes.

Recently, through systematic theoretical modelling based on density functional theory, a new class of SSEs for LIBs, based on Li_6OSI_2 with a cubic double anti-perovskite structure, has been theoretically formulated by our group.[29] They are electrochemically compatible with Li anodes, together with superb conductivity for lithium ions owing to very low activation energy for ion transport. The existence of unbroken three-dimensional (3D) networks for superfast Li^+ diffusion is particularly attractive, as the materials are thus free of concerns of crystalline orientations. It is therefore desirable to examine whether such a new phase structure would apply to SIBs, through complete substitution of Li by Na.

Here in this work, we have carried out extensive theoretical investigation of Na_6SOI_2-based materials, covering thermodynamic and dynamic stabilities, ion transport, and electrochemical compatibility with electrodes. It is found that double anti-perovskite Na_6SOI_2 is thermodynamically and dynamically stable and has ultra-fast Na^+ conductivity with a very small activation barrier of 0.21 eV. Through a moderate excess of Na while maintaining overall charge neutrality, an even lower activation energy of 0.16 eV is achieved for $Na_{25}S_5O_4I_7$, which is essential to obtain high ionic conductivity at and even well below room temperature. An outstanding Na^+ ion conductivity of 10.36 mS cm^{-1} at room temperature and 1.79 mS cm^{-1} even at -50 °C is then obtained. Besides, this new class of SSEs is electrochemically compatible with Na anodes, without any anode interphase to be energetically favoured. Such a low-cost and environmentally friendly material system is expected to provide a promising candidate to develop all-solid SIBs without safety concerns.

Methods

Theoretical calculations were performed using the Vienna Ab Initio Simulation Package (VASP),[30,31] with ionic potentials including the effect of core electrons being described by the projector augmented wave (PAW) method.[32,33] In this work, the Perdew–Burke–Ernzerhof (PBE) GGA exchange–correlation (XC) functionals[34,35] were used to study the structural stabilities in the Na_3AX family (A: chalcogen; X: halogen). For geometric relaxation of structures, summation over the Brillouin Zone (BZ) was performed with $3 \times 3 \times 3$ and $5 \times 5 \times 5$ Monkhorst–Pack k-point meshes for conventional and primitive cells, respectively, with k-point intervals being limited below 0.04 Å^{-1}.[36] A plane-wave energy cutoff of 600 eV was used in all calculations. All structures were geometrically relaxed until the total force on each ion was reduced below 0.01 eV Å^{-1}.[37–39] For calculations of electronic energy band structures, we used the HSE06 functional to predict more accurate values of band gaps.[40,41] We employed a convergence criterion of 10^{-6} eV, suitable for electronic self-consistent cycles.

The universal structure predictor (USPEX)[42,43] based on energy minimization was employed to predict stable or metastable structures for any given compositions. For each composition, a population of 200 possible structures was randomly created with varied symmetries in the first generation. When the full structural relaxation was reached, the most stable and metastable structures, through the comparison of enthalpy of formation, were placed into the next generation. Afterwards, each subsequent generation was created through heredity, with lattice mutation and permutation operators being applied and assessed energetically for the selection of a population of 60 for the next run. The USPEX would continue screening the structures until the most stable configuration remained unchanged for further 20 generations to safeguard the global equilibrium.[44]

The energy (enthalpy) of formation for each $Na_aS_bO_cI_dCl_e$ compound was defined with respect to the chemical potentials of the original composition as

$$E_f = E_{comp} - bE_{Na_2S} - cE_{Na_2O} - dE_{NaI} - eE_{NaCl} \qquad (1)$$

19844 | *J. Mater. Chem. A*, 2018, **6**, 19843–19852

This journal is © The Royal Society of Chemistry 2018

where E_{comp} is the total energy for the compound, E_f is the formation energy and E_{Na_2S}, E_{Na_2O}, E_{NaI}, and E_{NaCl} are the total energy for Na_2S, Na_2O, NaI, and $NaCl$ (we use the ground state stable structure as a reference for each element as listed in the Materials Project webpage https://www.materialsproject.org).

The phonon frequency spectrum of a theoretically predicted structure was used for examining its dynamic stability. The super-cell method in the PHONOPY package[45,46] was employed to perform the relevant frozen-phonon calculations based on harmonic approximation. The supercells of relaxed structures were used for the phonon calculations. The stability criterion was that the amplitude of imaginary frequency was less than 0.3 THz,[47,48] to accommodate acceptable numerical errors in phonon calculations.

Based on our recent tests, Ab initio molecular dynamics (AIMD) can be carried out for self-consistent description of the ion transport behaviour at varied temperatures and provide temperature-dependent data *via* statistical processes.[29,49,50] The resulting Arrhenius relationship for the diffusion coefficient D can then be correlated with ionic conductivity σ through the Nernst–Einstein relationship. To ensure a manageable AIMD analysis, simulation runs were performed on conventional cells of $Na_3A_aX_b$ with a time step of 2 fs in the NVT ensembles together with a Nosé–Hoover thermostat.[51] Correction of the MSD from artefactual errors due to the periodic boundary condition is necessary for dependable AIMD evaluation of D, using the "unwrapped" trajectories to help achieve significant improvement in sampling statistics from limited simulation data, typical for tractable AIMD runs.[29,49,50] Each AIMD run lasted for 80 ps after a pre-equilibrium run of 10 ps. In order to shorten the simulation time, elevated temperatures of 600 to 1200 K were employed to accelerate the ion hopping process.

Results and discussion

Initial compositional screening based on tolerance factors

Based on the Goldschmidt law, the ionic radius tolerance factor for an anti-perovskite phase Na_3AX can be defined as[52]

$$t = (R_{Na} + R_X)\big/\sqrt{2}(R_{Na} + R_A), \qquad (2)$$

where t should be in the range from 0.8 to 1 to stabilize an anti-perovskite structure. When the chalcogen site is occupied by O^{2-}, the smaller O^{2-} radius requires the X site occupied by a smaller filler to meet the tolerance factor, with Na_3OCl (0.83), Na_3OBr (0.87), and Na_3OI (0.94) compounds (with values in brackets being the tolerance factor) to satisfy the tolerance factor criterion to sustain the anti-perovskite structure. We learnt from recent work that the major hindrance for the transport of alkali ions in an anti-perovskite phase lithium chalcogenide arises from the electrostatic interaction between lithium and the chalcogen ions in the Li_6A octahedral units, so that replacing oxygen with other chalcogen species of lower electronegativity, *e.g.* S, helps promote the diffusion of alkali ions.[29] Unfortunately, the tolerance factor for Na_3SX ($X = Cl^-$, Br^-) is 0.7 and 0.74, respectively, being smaller than the lower limit of 0.8 due to the larger radius of S^{2-}. In order to increase

the tolerance factor of such sodium sulphides, we need to consider mono-valent anions with a larger ionic radius to fill the halogen site X. For example, when the X site is occupied by I^-, the tolerance factor of Na_3SI is increased to 0.8. Furthermore, an anion group of BF_4^- is also considered owing to its even bigger ionic radius (>10% *vs.* halogen anions), which helps lift the tolerance factor up to 0.85. Overall, for sodium sulfides, rather limited choices exist, *i.e.* Na_3SI and Na_3SBF_4, to satisfy the basic tolerance factor criterion for a stable anti-perovskite phase.

On the other hand, through alternating the occupancy of the A site by O and S, tolerance factors can be significantly enhanced when a smaller halogen ion occupies the X site, leading to double-anti-perovskite structural configurations.[29] The tolerance factor for a double-anti-perovskite structure based on the mixed occupancy of the A site is defined as the weighted sum of $R_{mixed} = (1 - x)R_1 + xR_2$, with x being the mole fraction of one anti-perovskite phase and $(1 - x)$ the molar fraction for the other.[29] It was demonstrated in the case of lithium halogen–chalcogenide that filling the X-site in such double-anti-perovskite phases helps widening the overall pathways for the transport of alkali ions.[29] Thus, the basic consideration is to utilize the mixed occupancy of the A site by S and O, together with introduction of smaller halogen anions such as Cl on the X site. For example, the chemical composition $Na_9S_2OI_2Cl$ can be considered as a mixture of the Na_3SI (0.8) and Na_3OI (0.94) phases with a mole ratio of 2 : 1, leading to a weighted tolerance factor of 0.81. Similarly, a series of chemical compositions Na_3OCl (0.83),[52,53] Na_3SI (0.8), Na_3SBF_4 (0.85), Na_6SOI_2 (0.87), Na_6SOICl (0.815), $Na_9S_2OI_3$ (0.85), and $Na_9S_2OI_2Cl$ (0.81) have thus been initially identified in line with the tolerance factor, as listed in Table 1.

Global search for low-energy structural configurations

The stable/metastable structures in each Na_3AX phase through isovalent replacement of either the chalcogen A site or the halogen X site are identified, using the USPEX method for global energy minimization of each chemical configuration.[42,43] Such a theoretical approach is particularly useful when little information is known about phase structures in a new material

Table 1 Tolerance factors from the Goldschmidt rule. Those in the range from 0.8 to 1 are emboldened

Ions and ionic radius (Å)	Tolerance factor	
	1 : 1	2 : 1
Na(1.02), O (1.4), Cl (1.81)	0.83	
Na(1.02), O (1.4), I (2.2)	**0.94**	
Na(1.02), S (1.84), Cl (1.81)	0.7	
Na(1.02), S (1.84), I (2.2)	**0.8**	
Na(1.02), S (1.84), BF_4(2.43)	**0.85**	
Na(1.02), O (1.4),BF_4(2.43)	1.008	
{Na(1.02), S (1.84), Cl (1.81), Na(1.02), O (1.4), Cl (1.81)}	0.765	
{Na(1.02), S (1.84), I (2.2), Na(1.02), O (1.4), I (2.2)}	**0.87**	**0.85**
{Na(1.02), S (1.84), I (2.2), Na(1.02), O (1.4), Cl (1.81) }	**0.815**	**0.81**
{Na(1.02), S (1.84), Cl (1.81),Na(1.02), O (1.4), I (2.2)}	**0.82**	

This journal is © The Royal Society of Chemistry 2018

J. Mater. Chem. A, 2018, **6**, 19843–19852 | **19845**

system to be formulated, so that potential phase structures can be predicted with associated properties simulated at 0 K.

Na$_3$SI has a typical characteristic as an anti-perovskite phase as shown in Fig. S1(a),† where the Na$_6$S octahedral unit is on the corners of a cubic frame, leaving I$^-$ sitting at the body center and thus leading to an overall lattice symmetry of $PM\bar{3}M$(221). With a larger BF$_4^-$ ion filling the centre of the cube of the Na–S framework, a significantly different configuration of Na$_3$SBF$_4$ appears with a quite low symmetry of (CM(8)) which has the lowest energy in this composition. This loss of high symmetry is caused by the structural transition associated with BF$_4^-$, as is shown in the largely distorted configuration presented in Fig. 1(a). The three F$^-$ ions still bond with B^{+3} and the fourth F$^-$ ion is taken away to bond with Na$^+$. The metastable Na$_3$SBF$_4$_2 with the same chemical composition exhibits the main characteristic of the anti-perovskite phase, slightly losing symmetry to $R3M$(160) (Fig. S1(b)).†

It is encouraging to note that the stable structure gains higher symmetry when half of the O site is replaced by S, with Na$_6$SOI$_2$ having a face-centered cubic space group ($FM\bar{3}M$) instead of a primitive cubic structure, a typical double-anti-perovskite phase made of alternating Na$_6$O and Na$_6$S octahedrons over a face-centered cubic lattice as shown in Fig. 1(b).

Through partial Cl substitution of I or higher O site replacement by S, the crystalline symmetry for the stable phase becomes lower. For example, for Na$_6$SOICl in Fig. 1(c), with half I sites taken by Cl, the stable structure is a tetragonal phase ($\bar{I}4M2$), which is largely similar to the structure of Na$_6$SOI$_2$, except for an elongated c axis with respect to the a-axis. The stable configuration of Na$_9$S$_2$OI$_2$Cl, on the other hand, is of rather low monoclinic symmetry (CM(8)), corresponding to its marginal tolerance factor of 0.81 (Fig. 1(d)). Meanwhile, a metastable configuration next to the stable phase of this composition, Na$_9$S$_2$OI$_2$Cl_2, still inherits the main feature of the anti-perovskite phase made of layered Na$_6$O or Na$_6$S octahedrons as shown in Fig. 1(e). Two connected layers of Na$_6$S octahedrons are sandwiched between layers of Na$_6$O octahedrons. Besides, the sites of halogen are off-centred, located at the middle point between Na on the vertices of neighbouring Na$_6$S octahedron units. Similarly, the metastable phase of Na$_9$S$_2$OI$_3$ exhibits separated layers made of Na$_6$O and Na$_6$S

Table 2 Lattice parameters and symmetry groups of various configurations (Confs) from USPEX global search

Confs	a	b	c(Å)	α	β	γ(°)	Symmetry
Na$_3$OCl	4.34	4.34	4.34	90	90	90	$PM\bar{3}M$(221)
Na$_3$SI	5.16	5.16	5.16	90	90	90	$PM\bar{3}M$(221)
Na$_3$SBF$_4$	6.56	6.88	9.74	90	142.81	90	CM8
Na$_3$SBF$_4$_2	7.28	7.28	9.07	90	90	120	$R3M$(160)
Na$_6$SOI$_2$	9.96	9.96	9.96	90	90	90	$FM\bar{3}M$(225)
Na$_6$SOICl	6.93	6.93	9.72	90	90	90	$\bar{I}4M2$(119)
Na$_9$S$_2$OI$_3$	7.18	7.18	8.84	90	90	120	$P\bar{3}M1$(164)
Na$_9$S$_2$OI$_2$Cl	11.46	11.46	7.36	83.5	83.5	23.18	CM8
Na$_9$S$_2$OI$_2$Cl_2	6.99	6.99	9.06	90	90	120	$P3$(143)

octahedrons, respectively, as shown in Fig. S1(c),† with the position of I also being off-centred. Table 2 summarizes the USPEX search results for stable or metastable structures with geometrically relaxed lattice parameters for the compositions covering Na$_3$OCl (an experimentally fabricated compound), Na$_3$SI, Na$_3$SBF$_4$ (stable), Na$_3$SBF$_4$_2 (metastable), Na$_6$SOI$_2$, Na$_6$SOICl, Na$_9$S$_2$OI$_3$, Na$_9$S$_2$OI$_2$Cl (stable), and Na$_9$S$_2$OI$_2$Cl_2 (metastable).

Fig. 2 compares the energies of formation per atom for each stable/metastable configuration at zero kelvin. Here, we follow the convention to formulate the energy of formation with respect to the associated equilibrium constituent phases or precursors (e.g. Na$_2$O, Na$_2$S, NaCl, NaI, and NaBF$_4$). We find that the energy of Na$_3$SBF$_4$ with the symmetry of CM(8) is lower than that of mixed constituent phases (Na$_2$S and NaBF$_4$) at 0 K. Similar situations are observed for the compounds of Na$_3$OCl (vs. Na$_2$O + NaCl) and Na$_6$SOI$_2$ (vs. Na$_2$O + Na$_2$S + 2NaI). The stability is compromised when the chalcogen site is occupied by more S than O, or Cl partially occupies the halogen sites, with compound energies being bigger than that of the constituent phases. That is to say, in terms of energies, Na$_3$SI > Na$_2$S + NaI, Na$_9$S$_2$OI$_3$ > 2Na$_2$S + Na$_2$O + 3Na, Na$_6$SOICl > Na$_2$S + Na$_2$O + NaI + NaCl, Na$_9$S$_2$OI$_2$Cl or Na$_9$S$_2$OI$_2$Cl_2 > 2Na$_2$S + Na$_2$O + 2NaI + NaCl.

Dynamic stability

Dynamic stabilities of the fully relaxed structures of the energetically stable configuration at 0 K from USPEX search are
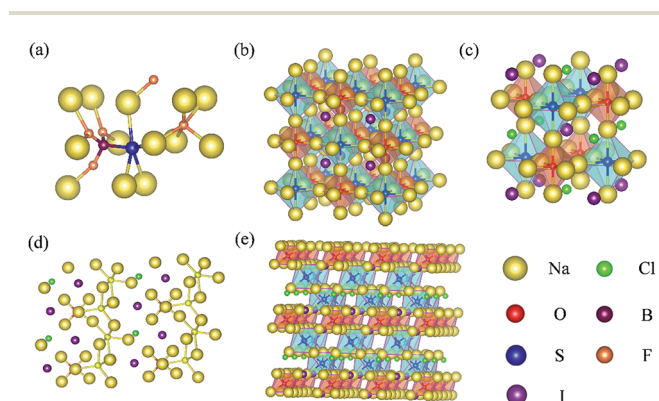

Fig. 1 (a)Na$_3$SBF$_4$, (b)Na$_6$SOI$_2$, (c)Na$_6$SOICl, (d) Na$_9$S$_2$OI$_2$Cl and (e) Na$_9$S$_2$OI$_2$Cl_2, obtained from global USPEX search.
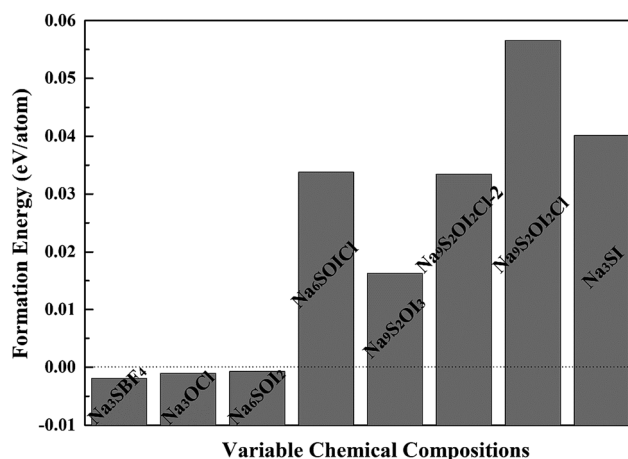

Fig. 2 The formation energies for Na$_3$AB-based alloys with respect to stable constituent phases.

checked through examining the characteristics of their phonon band structures. A phase is dynamically stable when no phonon bands are associated with imaginary frequencies. Fig. 3(a)–(e) show calculated phonon band structures for various supercells (around 30 to 80 atoms) of (a) Na_3SBF_4 ($2 \times 2 \times 2$), (b) Na_6SOI_2 ($2 \times 2 \times 2$), (c) Na_6SOICl ($2 \times 2 \times 2$), (e) $Na_9S_2OI_2Cl$ ($1 \times 1 \times 2$), and (f) $Na_9S_2OI_2Cl\_2$ ($2 \times 2 \times 2$), where the grey lines indicate zero frequency. The cyan lines represent the acceptable stability margin of -0.3 THz in phonon calculations, which is due to the high sensitivity of the relaxed structures to remnant stress. The employment of such a stability margin is useful when carrying out expensive phonon calculations on systems containing computationally manageable numbers of atoms. The existence of an imaginary frequency below the threshold of -0.3 THz indicates dynamic instability. It is seen from Fig. 3 that the criterion of a margin of -0.3 THz is satisfied for all the fully relaxed structures, suggesting that all these structures can be considered to be dynamically stable. In contrast, large imaginary frequencies emerge below the criterion of -0.3 THz for the associated compounds of (a) Na_3SI, (b) $Na_3SBF_4\_2$, and (c) $Na_9S_2OI_3$ as shown in Fig. S2,† which implies that they are dynamically unstable and less likely to occur in nature. It is worth stressing that the same convergence criterion is used to relax structures for phonon calculations so that self-consistency is maintained in the resulting phonon band structures. As a result, only Na_3SBF_4, Na_6SOI_2, Na_6SOICl, $Na_9S_2OI_2Cl$ and $Na_9S_2OI_2Cl\_2$ are stable both energetically and dynamically, while Na_3SI, $Na_3SBF_4\_2$, and $Na_9S_2OI_3$ do not meet the dynamical stability criterion (meaning such structures are likely to collapse due to mechanical instability).

Stability with respect to constituent stable phases

We then checked the stability of the above identified ternary or quaternary compounds with respect to stable constituent phases. Firstly, we construct pseudo-ternary phase diagrams of Na_6SOI_2 at 0 K, Fig. 4(a), based on energies of formation, with

reference to its potential constituent candidates such as those collected in the Materials Project (MP). It shows that pseudo-ternary phase diagrams of Na_6SOI_2 at 0 K are less stable with respect to that of its constituent phases of Na_2S and Na_4OI_2, with Na_4OI_2 being more stable than $Na_2O + 2NaI$.[53] Due to its energies of formation being less negative than the linear combinations of its respective constituent phases, energetically it tends to decompose into constituent structures at the ground state.

$$Na_6SOI_2 \rightarrow Na_4OI_2 + Na_2S \qquad (3)$$
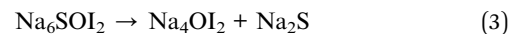
We now examine the thermal effects on Gibbs free energies of compounds within the quasi-harmonic approximation to consider the phonon entropy, shown in Fig. 4(d). The free energies for Na_6SOI_2 and Na_4OI_2 can be calculated against their stable constituent compounds using the following:

$$\Delta G_{Na_4OI_2} = G_{Na_4OI_2} - G_{Na_2O} - 2G_{NaI} \qquad (4)$$

$$\Delta G_{Na_6SOI_2} = G_{Na_6SOI_2} - G_{Na_4OI_2} - G_{Na_2S} \qquad (5)$$

where all energetically stable constituents such as Na_2O, Na_2S, Na_4OI_2 and NaI are found to be also dynamically stable.

According to calculated Gibbs free energies in the range from 352 to 438 K, Na_6SOI_2 is stable with respect to Na_4OI_2 and Na_2S, with its formation energy getting more negative against increasing temperature, as shown in Fig. 4(b). As the temperature rises to 438 K, Na_4OI_2 turns energetically unstable with respect to Na_2O and NaI, but Na_6SOI_2 is still stable with reference to Na_2O, Na_2S and NaI over 438 K, as shown below:

$$\Delta G_{Na_6SOI_2} = G_{Na_6SOI_2} - G_{Na_2O} - G_{Na_2S} - 2G_{NaI} \qquad (6)$$

Fig. 4(c) shows the stable phase diagram above 438 K, since the cubic Na_6SOI_2 phase is energetically favoured with respect to either the combination of Na_4OI_2 and Na_2S in the range of 352–438 K, or the combination of Na_2O, Na_2S and NaI above 438 K as shown in Fig. 4(d). This manifests that Na_6SOI_2 will be energetically stable above 352 K (79 °C). It is worth pointing out that all recently discovered solid-state electrolytes such as the well-known LGPS[17] and Li_3OCl[54] are only stable at elevated temperatures. Like the double anti-perovskite phase from this work, the feasibility of their synthesis lies in their capability to be entropically stabilized at moderately elevated temperatures. In practice, one can achieve sufficient mixing of the chemical species with the assistance of long-range diffusion at a high temperature above T_c, followed by quick cooling or quenching the products adequately to avoid the nucleation and growth of low-temperature stable phases, since cooling such materials through a range of low temperatures below T_c does not tend to permit long-range diffusion of any chemical species other than Na^+.[55]

On the other hand, through similar Gibbs free energy calculations, Na_6SOICl, $Na_9S_2OI_2Cl$ and $Na_9S_2OI_2Cl\_2$ are demonstrated as energetically unstable over a wide temperature range, as displayed in Fig. S3(a)–(c).† One can see that the Gibbs
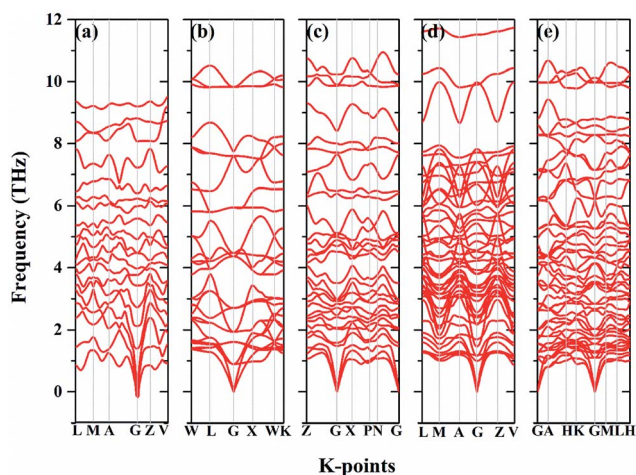

Fig. 3 Calculated phonon band structures of the stable structures of (a)Na_3SBF_4, (b)Na_6SOI_2, (c)Na_6SOICl, (d) $Na_9S_2OI_2Cl$ and (e) $Na_9S_2OI_2Cl\_2$.

This journal is © The Royal Society of Chemistry 2018

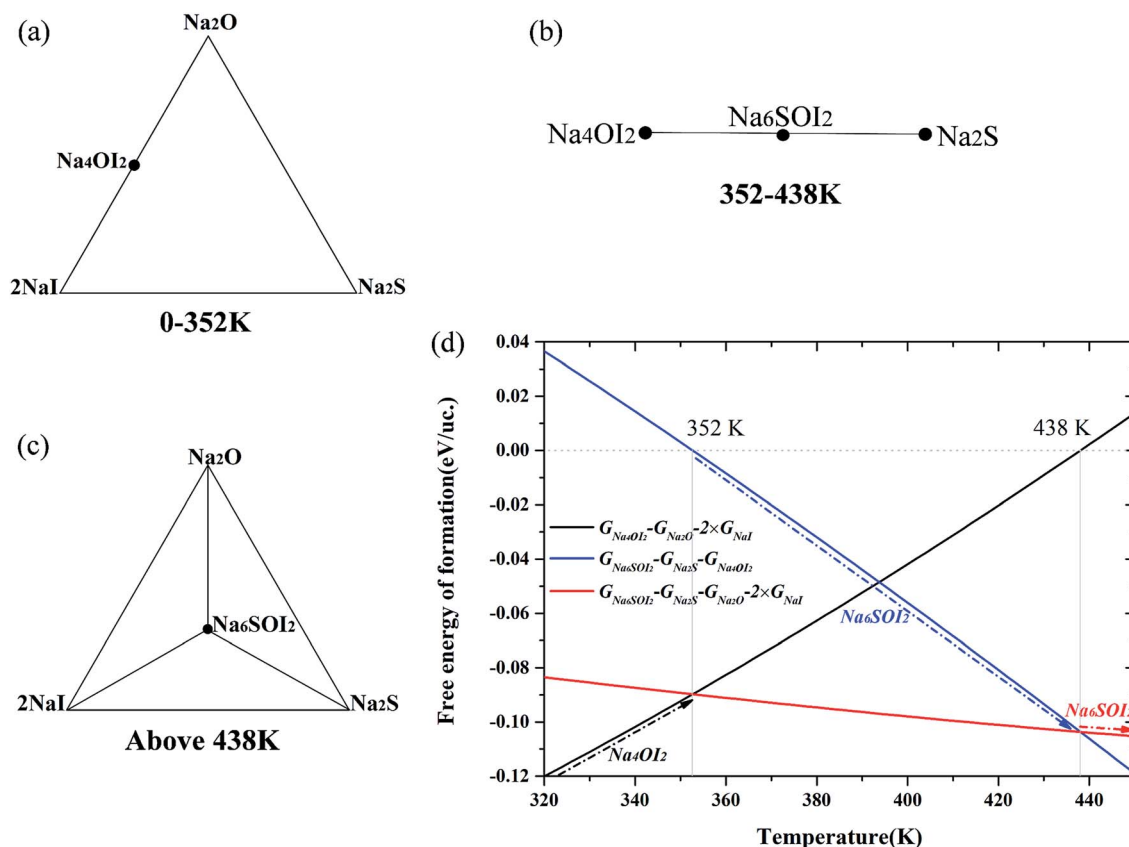J. Mater. Chem. A, 2018, 6, 19843–19852 | 19847

Fig. 4 (a–c) Phase diagrams of Na_6OSI_2 at different temperature ranges, with filled circles representing stable compounds. The phase transition process is shown in (d), in which the dotted arrowed lines indicate the stable phases in each specific temperature region.

free energy change ΔG for Na_6SOICl, $Na_9S_2OI_2Cl$ and Na_9S_2-OI_2Cl_2, with respect to their constituent compounds, is always larger than zero. The only exception is Na_3SBF_4 (Fig. S3(d)†), which is energetically favoured against the constituent mixture of $Na_2S + NaBF_4$. In summary, through extensive configuration screening, it was found that only two compounds, Na_3SBF_4 and Na_6SOI_2, satisfy both the energetic and dynamic stability criteria.

Electrochemical compatibility with Na anodes

The electrochemically compatible window with Na metal anodes can be examined according to interfacial reactions against Na uptake per formula unit (f.u.) of solid electrolyte. The average electrochemical potential, $\bar{V}_{\bar{A}B}$, for the transition between state A ($Na_x\prod$) and state B ($Na_{x+\Delta x}\prod$), with reference to electrochemical potential for the sodium metal is related to total energies (E_{total}) as follows:

$$\overline{V}_{A \to B} = -1/z \left\{ \left[E_{total}\left(Na_{x+\Delta x}\prod \right) - E_{total}\left(Na_x \prod \right) \right] / \Delta x - E_{total}(Na) \right\} \quad (7)$$

where x is the number of Na in the formula unit of $Na_x\prod$, charge value $z = 1$ for Na^+, Δx is the change in the number of Na atoms, and $\prod$ refers to the collection of other constituents. Again, energetically stable constituent phase structures for each Na level were identified from the USPEX global search.

Fig. 5 shows the plot of the voltage above Na/Na^+ against the Na uptake per formula unit of Na_6SOI_2. The solid electrolyte undergoes reduction and uptake of Na next to the alkali metal anode (Na rich side) at low voltage, while at high voltage (Na poor side), the electrolyte is oxidized to deplete Na. In view of the electrochemical window according to the associated equilibrium phases at 0 K, the wide intrinsic electrochemical window of Na_6SOI_2 spans from 0.0 to 1.5 V *vs.* Na, wherein the SSE without an energetic driver to form any Na_6SOI_2 will be electrochemically stable against the Na anode without any interphase between them. In contrast, the widths of intrinsic electrochemical windows for known Na^+ SSEs are quite narrow, *e.g.* the anode solid interphase (ASI). This is attributed to the higher stability of Na_6SOI_2 than its constituent binary phases and the lack of intermediate products between Na_2S, Na_2O, NaI and Na, so that Na_3SbS_4 (1.36–2.53 V), $Na_{10}GeP_2S_{12}$ (1.25–1.70 V), $Na_{10}SnP_2S_{12}$ (1.25–1.82 V), Na_3PSe_4 (1.39–1.61 V), and Na_3PS_4 (1.49–1.55 V) due to high reduction potential *vs.* Na. The wide electrochemical window between Na_6SOI_2 and Na is highly desirable for practical application, without the concern of formation of potentially detrimental ASI to consume active lithium sources or to cause a significant increase in interfacial resistance. Besides, the maximum oxidation potential for sodium depletion equals 2.55 V without O_2 gas being generated, which is higher than that of the $Na_{10}GeP_2S_{12}$ family (2.16 V), Na_3PSe_4 (2.05 V), and Na_3PS_4 (1.76 V), and is similar to that of

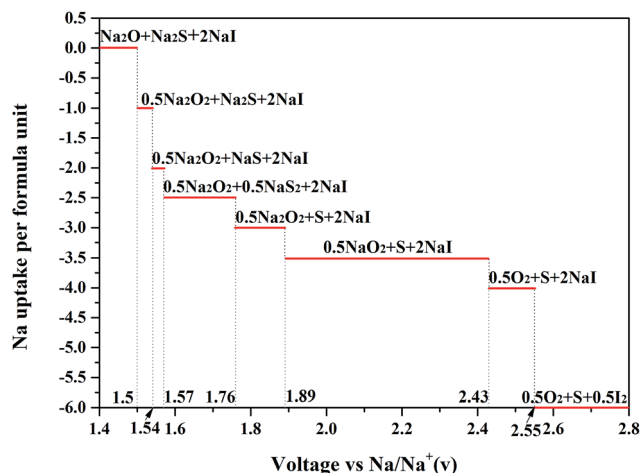19848 | *J. Mater. Chem. A*, 2018, **6**, 19843–19852

This journal is © The Royal Society of Chemistry 2018

Fig. 5 Plot of Na uptake per formula unit of solid electrolyte (red solid) against voltage *vs.* Na/Na$^+$ for Na$_6$SOI$_2$. The text indicates the predicted phase equilibria in the corresponding regions at 0 K.

Na$_3$SbS$_4$ with 2.57 V as shown in Fig. 6. The corresponding compositions on the anode solid interphases for each SSE are listed in Table S1.† It is seen that only Na$_6$SOI$_2$ is free of interphase with the Na anode, and its width of electrochemical window is highest among the other SSEs. It could be helpful to promote the working voltage of the full-cell and contribute to maintain intrinsic phases to achieve fast transport of Na$^+$ ions in the electric field.

Na$^+$ transportation through AIMD

As established recently, diffusion coefficients (*D*) of alkali ions in solids can be readily quantified using ab initio molecular dynamics (AIMD),[56,57] through correlation of diffusion coefficients with mean square displacement (MSD).[29,50,51] The diffusion data are presented in Fig. 7, showing the logarithmic value of *D versus* the reverse of temperature 1000/*T*. The linear correlations demonstrate typical Arrhenius relationships,
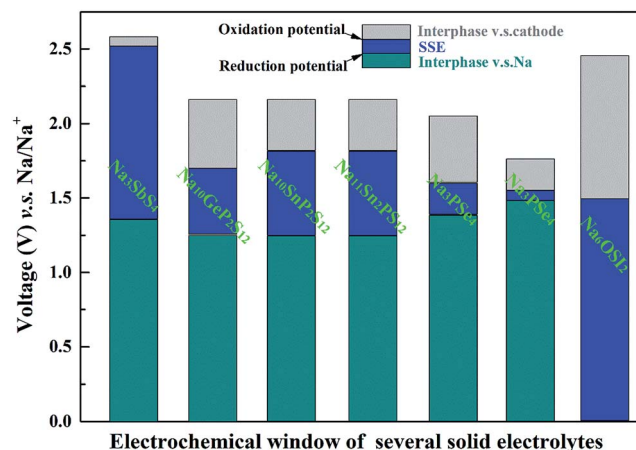
which result in activation energies and extrapolated lower temperature data.

In reality, both vacancy and interstitial mechanisms for alkali ion transportation would exist in an electrolyte layer. On the Na-rich side of the Na|SSE interface, excess Na$^+$ tends to lead to interstitial alkali ions, meanwhile Na$^+$ vacancies tend to appear next to the SSE|cathode interface.[58] The vacancy mechanism for sodium transportation in Na$_6$SOI$_2$ is assessed by taking away a Na$^+$ ion in four unit-cells, *i.e.* Na$_{23}$S$_4$O$_4$I$_8$. Moderate excess sodium with the constraint of charge neutrality is represented by Na$_{25}$S$_5$O$_4$I$_7$. For the anti-perovskite Na$_3$OCl, the AIMD data based on the vacancy mechanism predict an activation barrier E_a = 0.41 eV (wine red square line in Fig. 7) which agrees with the value of 0.428 obtained from the NEB method,[53] while the associated ionic conductivity is quite low, being only 2.12 × 10^{-3} mS cm^{-1} (listed in Table 3) in the same order of 10^{-3} mS cm^{-1} of reported experimental values.[53] In the case of Na$_6$SOI$_2$, its ionic activation barrier coming from the vacancy mechanism is reduced significantly down to 0.21 eV, decreased about 50% compared with that of Na$_3$OCl. The main S effect on partially substituting O lies in lattice softening, which is owing to weakened bonding to the chalcogen anion within each S-centred octahedron. This in turn leads to lattice enlargement and widened diffusion channels for Na$^+$ transportation, which is in principle consistent with recent work on
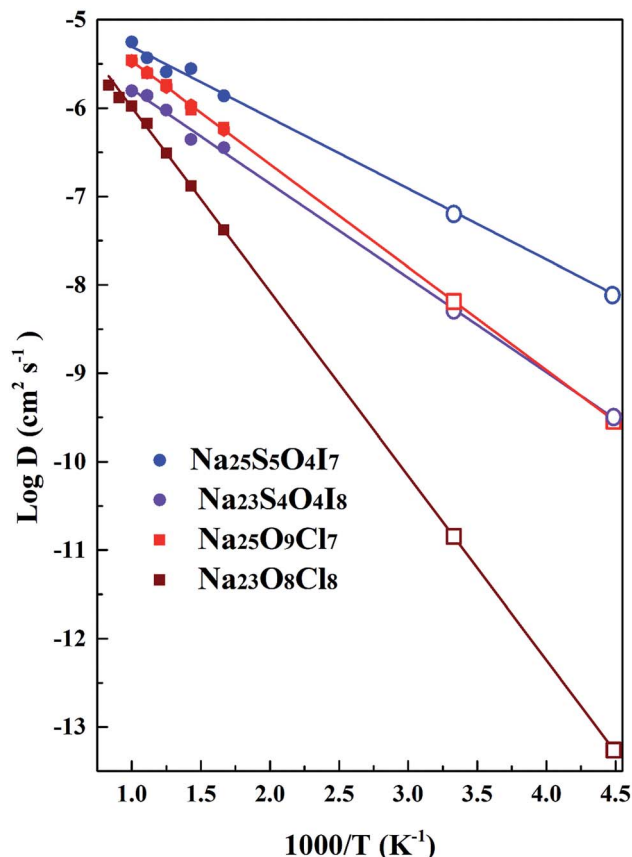

Fig. 7 Diffusion coefficients for sodium ions from AIMD simulation. The *D* values at room temperature and −50 °C are presented by open patterns on the right side of the figure panel.

Fig. 6 The oxidation potential and reduction potential for various SSEs. The gray area represents the interphase with the cathode or Na anode. The blue area is the intrinsic electrochemical window.

This journal is © The Royal Society of Chemistry 2018

J. Mater. Chem. A, 2018, **6**, 19843–19852 | **19849**

Table 3 Summary of data for ionic diffusion and conductivity of this work and reported SSEs from the literature

System	E_a (eV)	Arrhenius prefactor (cm^{-2} s^{-1})	ρ (10^{-23} cm^{-3})	$D_{300\,K}$ (cm^{-2} s^{-1})	Σ (mS cm^{-1}) 300 K	223 K
Na$_{23}$O$_8$Cl$_8$	0.41	1.25×10^{-4}	17.968	1.413×10^{-11}	2.12×10^{-3}	8.44×10^{-6}
Na$_{25}$O$_9$Cl$_7$	0.23	4.95×10^{-5}	17.968	6.5×10^{-9}	1.376	6.3×10^{-2}
Na$_{23}$S$_4$O$_4$I$_8$	0.21	1.91×10^{-5}	24.3719	5.30×10^{-9}	0.8	4.8×10^{-2}
Na$_{25}$S$_5$O$_4$I$_7$	0.16	3.14×10^{-5}	24.3719	6.64×10^{-8}	10.36	1.79
Na$_3$SBF$_4$	0.27	6.59×10^{-5}	13.0952	1.7×10^{-9}	0.27	8×10^{-3}
Na$_3$SbS$_4$ (ref. 23)	0.22[Exp]				1[Exp]	
Na$_{10}$GeP$_2$S$_{12}$ (ref. 16)	0.2[Exp]				4.7[Exp]	
Na$_{10}$SnP$_2$S$_{12}$ (ref. 16)	0.317				0.94	
	0.36[Exp]				0.4[Exp]	
Na$_{11}$Sn$_2$PS$_{12}$ (ref. 16)	0.2				2.4	
	0.25[Exp]				1.4[Exp]	
Na$_3$PSe$_4$ (ref. 20)	0.28[Exp]				0.11[Exp]	
Na$_3$PS$_4$ (ref. 19)	0.2[Exp]				0.2[Exp]	

double anti-perovskite Li$^+$ ion conductors.[29] The ionic conductivity of 0.8 mS cm^{-1} is increased to nearly a thousand times over that of Na$_3$OCl at room temperature.

Recent theoretical studies of alkali transportation in lithium sulphides indicated that moderate off-stoichiometric compositions help significantly promote sodium ion transportation in cubic argyrodite phases.[29,50,51] Such an effect also holds true in the case of sodium ions, so that extraneous Na$^+$ together with chalcogen substitution for halogen to maintain overall charge neutrality leads to significant enhancement of ionic conductivity. Moderate Na$^+$ excess in Na$_{25}$S$_5$O$_4$I$_7$ delivers remarkable reduction in the activation energy down to 0.16 eV, which is about one-third lower in comparison to those of the phases of Na$_{25}$O$_9$Cl$_7$ (0.23 eV) and Na$_{23}$S$_4$O$_4$I$_8$ (0.21 eV). This confirms that the presence of interstitial Na$^+$ leads to more effective

enhancement of Na$^+$ transport than relying solely on Na$^+$ vacancies. The Na$^+$ ion trajectory density is highly overlapped as shown in Fig. 8(d), while the trajectory for single Na$^+$ ions in long range diffusion can be observed in Fig. S5(b).† The diffusion data for various alloys are listed in Table 3 for comparison with data obtained from reported data from the literature. From direct comparison, we can find that Na$_{25}$S$_5$O$_4$I$_7$ has the largest Arrhenius prefactor with high probability for Na$^+$ hopping. When excess Na$^+$ appears at an interstitial site in the neighbourhood of lattice Na$^+$, the attractive interaction of O/S on Na$^+$ would be weakened due to the charge screening effect. This also provides a shorter jumping distance for an interstitial Na$^+$ ion to fill a vacancy on such neighbouring lattice sites. The combined effects thus result in a very low activation energy of 0.16 eV for Na$_{25}$S$_5$O$_4$I$_7$, which is essential to promote superb Na$^+$ transportation, achieving an ionic conductivity of 10.36 mS cm^{-1} at room temperature. This very low activation energy even offers 1.79 mS cm^{-1} ionic conductivity at a very low temperature of $-50\,°C$. This suggests great potential to utilise the current solid
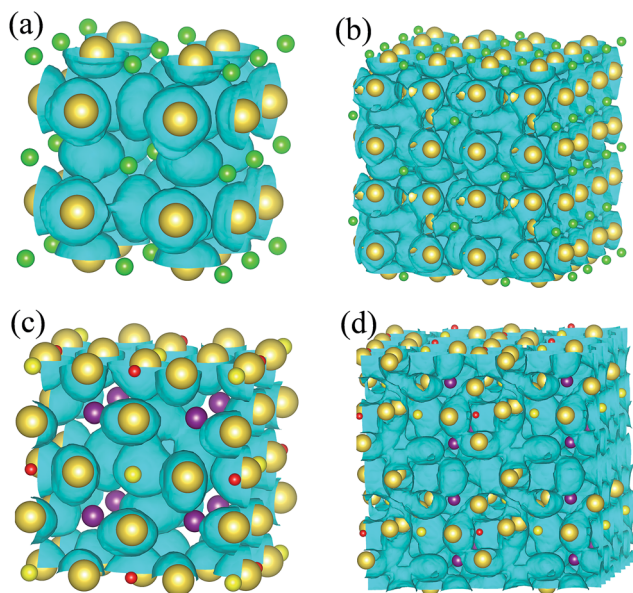

Fig. 8 The diffusion paths of sodium ions for (a) Na$_{23}$O$_8$Cl$_8$, (b) Na$_{25}$O$_9$Cl$_7$, (c) Na$_{23}$S$_4$O$_4$I$_8$, and (d) Na$_{25}$S$_5$O$_4$I$_7$, over a simulation time of 90 ps.
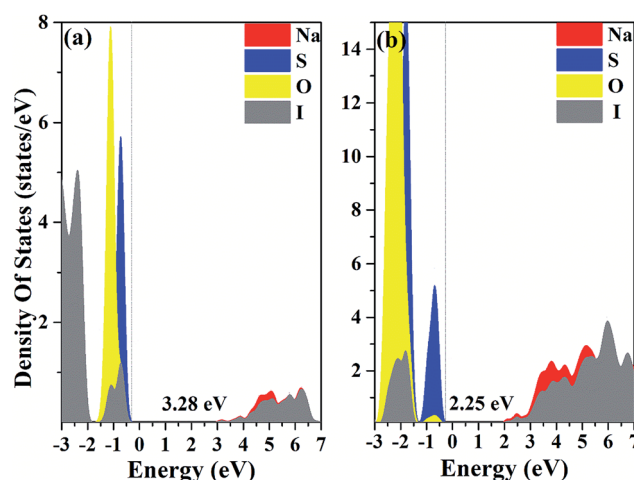
Fig. 9 The projected density of states calculated using the HSE06 functional: (a) Na$_6$SOI$_2$; (b) Na$_{25}$S$_5$O$_4$I$_7$.

19850 | J. Mater. Chem. A, 2018, 6, 19843–19852

This journal is © The Royal Society of Chemistry 2018

electrolyte system for safe SIBs over a very wide operating temperature range.

Bandgap

While an SSE should be highly conductive to Na^+ ions, it should be insulating for the conduction of electrons to avoid internal discharging. Fig. 9 summarizes the density of states (DOS) for the ion conductors of interest to this work, using the HSE06 screened hybrid functional for improved accuracy in band structure calculations, by accounting for some non-local effects in the exchange–correlation functional. It can be seen that both materials of interest are insulating to electrons, due to the existence of rather large forbidden energy gaps between the valence band maximum (VBM) and conduction band minimum (CBM). Both the VBM and CBM are dominated by electron states of anions in all compounds. Moreover, the forbidden gap is shown to be mainly determined by the type of chalcogen species (O and S), so that the gap value is correlated with the overall bonding strength. The band gap of Na_6SOI_2 is 3.28 eV, and the charge neutrality in $Na_{25}S_5O_4I_7$ is shown to safeguard its intrinsic nature as a wide gap material (2.25 eV), without any defect states being present in the forbidden gap.

Conclusions

Superb Na^+ ion conductors have been identified through systematic modelling, leading to theoretical discovery of a double anti-perovskite Na_6SOI_2 phase, which is electrochemically compatible with sodium anodes.

AIMD simulation shows that moderate off-stoichiometric compositional deviation in the double-anti-perovskite phase leads to significant reduction of the activation barrier for Na^+ transportation. This includes moderate enrichment of Na ions together with chalcogen excess and halogen deficiency to maintain charge neutrality. This combined effect results in a very low activation energy of about 0.16 eV for $Na_{25}S_5O_4I_7$, making it particularly attractive for low temperature application in solid SIBs.

Conflicts of interest

There are no conflicts to declare.

Acknowledgements

Notes and references

1 M. Armand and J. M. Tarascon, *Nature*, 2008, **451**, 652–657.
2 B. Dunn, H. Kamath and J. M. Tarascon, *Science*, 2011, **334**, 928–935.
3 B. Scrosati, J. Hassoun and Y.-K. Sun, *Energy Environ. Sci.*, 2011, **4**, 3287.
4 Q. Wang, P. Ping, X. Zhao, G. Chu, J. Sun and C. Chen, *J. Power Sources*, 2012, **208**, 210–224.
5 N. Nitta, F. Wu, J. T. Lee and G. Yushin, *Mater. Today*, 2015, **18**, 252–264.
6 V. Palomares, P. Serras, I. Villaluenga, K. B. Hueso, J. Carretero-González and T. Rojo, *Energy Environ. Sci.*, 2012, **5**, 5884.
7 A. Eftekhari, *J. Power Sources*, 2004, **126**, 221–228.
8 X. Fan, R. R. Gaddam, N. A. Kumar and X. S. Zhao, *Adv. Energy Mater.*, 2017, **7**, 1700317.
9 Z. Wang and G. Shao, *J. Mater. Chem. A*, 2018, **6**, 6830–6839.
10 L. Zhang, L. Chen, X. Zhou and Z. Liu, *Adv. Energy Mater.*, 2015, **5**, 1400930.
11 H. Pan, Y.-S. Hu and L. Chen, *Energy Environ. Sci.*, 2013, **6**, 2338.
12 J.-Y. Hwang, S.-T. Myung and Y.-K. Sun, *Chem. Soc. Rev.*, 2017, **46**, 3529–3614.
13 T. Zhang, Y. Wang, T. Song, H. Miyaoka, K. Shinzato, H. Miyaoka, T. Ichikawa, S. Shi, X. Zhang, S. Isobe, N. Hashimoto and Y. Kojima, *Joule*, 2018, **2**, 1522–1533.
14 Q. Zhao, L. Pan, Y.-J. Li, L.-Q. Chen and S.-Q. Shi, *Rare Met.*, 2018, **37**, 497–503.
15 Y. Yang, Q. Wu, Y. Cui, Y. Chen, S. Shi, R. Z. Wang and H. Yan, *ACS Appl. Mater. Interfaces*, 2016, **8**, 25229–25242.
16 M. Tatsumisago, M. Nagao and A. Hayashi, *J. Am. Ceram. Soc.*, 2018, **1**, 17–25.
17 A. Kuhn, V. Duppel and B. V. Lotsch, *Energy Environ. Sci.*, 2013, **6**, 3548.
18 N. Kamaya, K. Homma, Y. Yamakawa, M. Hirayama, R. Kanno, M. Yonemura, T. Kamiyama, Y. Kato, S. Hama, K. Kawamoto and A. Mitsui, *Nat. Mater.*, 2011, **10**, 682–686.
19 Z. Zhang, E. Ramos, F. Lalère, A. Assoud, K. Kaup, P. Hartman and L. F. Nazar, *Energy Environ. Sci.*, 2018, **11**, 87–93.
20 W. D. Richards, T. Tsujimura, L. J. Miara, Y. Wang, J. C. Kim, S. P. Ong, I. Uechi, N. Suzuki and G. Ceder, *Nat. Commun.*, 2016, **7**, 11009.
21 A. Hayashi, K. Noi, N. Tanibata, M. Nagao and M. Tatsumisago, *J. Power Sources*, 2014, **258**, 420–423.
22 A. Hayashi, K. Noi, A. Sakuda and M. Tatsumisago, *Nat. Commun.*, 2012, **3**, 856.
23 S.-H. Bo, Y. Wang, J. C. Kim, W. D. Richards and G. Ceder, *Chem. Mater.*, 2015, **28**, 252–258.
24 L. Zhang, K. Yang, J. Mi, L. Lu, L. Zhao, L. Wang, Y. Li and H. Zeng, *Adv. Energy Mater.*, 2015, **5**, 1501294.
25 A. Banerjee, K. H. Park, J. W. Heo, Y. J. Nam, C. K. Moon, S. M. Oh, S.-T. Hong and Y. S. Jung, *Angew. Chem., Int. Ed.*, 2016, **55**, 9634–9638.
26 H. Wang, Y. Chen, Z. D. Hood, G. Sahu, A. S. Pandian, J. K. Keum, K. An and C. Liang, *Angew. Chem., Int. Ed.*, 2016, **55**, 8551–8555.
27 F. Lalère, J. B. Leriche, M. Courty, S. Boulineau, V. Viallet, C. Masquelier and V. Seznec, *J. Power Sources*, 2014, **247**, 975–980.

This journal is © The Royal Society of Chemistry 2018

J. Mater. Chem. A, 2018, **6**, 19843–19852 | **19851**

28 A. Inoishi, T. Omuta, E. Kobayashi, A. Kitajou and S. Okada, *Adv. Mater. Interfaces*, 2017, **4**, 1600942.

29 Z. Wang, H. Xu, M. Xuan and G. Shao, *J. Mater. Chem. A*, 2018, **6**, 73–83.

30 G. Kresse and J. Hafner, *Phys. Rev. B*, 1993, **47**, 558–561.

31 G. Kresse and J. Hafner, *Phys. Rev. B*, 1994, **49**, 14251–14269.

32 P. E. Blöchl, *Phys. Rev. B*, 1994, **50**, 17953–17979.

33 G. Kresse and D. Joubert, *Phys. Rev. B*, 1999, **59**, 1758–1775.

34 G. Kresse and J. Hafner, *Phys. Rev. B*, 1993, **48**, 13115–13118.

35 J. P. Perdew, K. Burke and M. Ernzerhof, *Phys. Rev. Lett.*, 1996, **77**, 3865–3868.

36 G. Shao, *J. Phys. Chem. C*, 2009, **113**, 6800–6808.

37 G. Shao, *J. Phys. Chem. C*, 2014, **112**, 18677–18685.

38 X. Han, K. Song, L. Lu, Q. Deng, X. Xia and G. Shao, *J. Mater. Chem. C*, 2013, **1**, 3736.

39 X. Han and G. Shao, *J. Mater. Chem. C*, 2015, **3**, 530–537.

40 J. Heyd, G. E. Scuseria and M. Ernzerhof, *J. Chem. Phys.*, 2003, **118**, 8207–8215.

41 J. Heyd, G. E. Scuseria and M. Ernzerhof, *J. Chem. Phys.*, 2006, **124**, 219906.

42 A. R. Oganov and C. W. Glass, *J. Chem. Phys.*, 2006, **124**, 244704.

43 C. W. Glass, A. R. Oganov and N. Hansen, *Comput. Phys. Commun.*, 2006, **175**, 713–720.

44 Z. Wang, B. Lei, X. Xia, Z. Huang, K. P. Homewood and Y. Gao, *J. Phys. Chem. C*, 2018, **122**, 2589–2595.

45 K. Parlinski, Z. Q. Li and Y. Kawazoe, *Phys. Rev. Lett.*, 1997, **78**, 4063–4066.

46 A. Togo, F. Oba and I. Tanaka, *Phys. Rev. B*, 2008, **78**, 134106.

47 T. D. Huan, V. N. Tuoc and N. V. Minh, *Phys. Rev. B*, 2016, **93**, 094105.

48 F. Brivio, J. M. Frost, J. M. Skelton, A. J. Jackson, O. J. Weber, M. T. Weller, A. R. Goñi, A. M. A. Leguy, P. R. F. Barnes and A. Walsh, *Phys. Rev. B*, 2015, **92**, 144308.

49 M. V. Agnihotri, S. H. Chen, C. Beck and S. J. Singer, *J. Phys. Chem. B*, 2014, **118**, 8170–8178.

50 Z. Wang and G. Shao, *J. Mater. Chem. A*, 2017, **5**, 21846–21857.

51 Z. Deng, Z. Zhu, I.-H. Chu and S. P. Ong, *Chem. Mater.*, 2016, **29**, 281–288.

52 C. H. Hendon, R. X. Yang, L. A. Burton and A. Walsh, *J. Mater. Chem. A*, 2015, **3**, 9067–9070.

53 Y. Wang, Q. Wang, Z. Liu, Z. Zhou, S. Li, J. Zhu, R. Zou, Y. Wang, J. Lin and Y. Zhao, *J. Power Sources*, 2015, **293**, 735–740.

54 M. H. Braga, J. A. Ferreira, V. Stockhausen, J. E. Oliveira and A. El-Azab, *J. Mater. Chem. A*, 2014, **2**, 5470–5480.

55 K. T. Lai, I. Antonyshyn, Y. Prots and M. Valldor, *J. Am. Chem. Soc.*, 2017, **139**, 9645–9649.

56 S. Shi, J. Gao, Y. Liu, Y. Zhao, Q. Wu, W. Ju, C. Ouyang and R. Xiao, *Chin. Phys. B*, 2016, **25**, 018212.

57 J. Gao, Y. Sh. Zhao, S. Q. Shi and H. Li, *Chin. Phys. B*, 2016, **25**, 018211.

58 A. C. Luntz, J. Voss and K. Reuter, *J. Phys. Chem. Lett.*, 2015, **6**, 4599–4604.

19852 | *J. Mater. Chem. A*, 2018, **6**, 19843–19852

This journal is © The Royal Society of Chemistry 2018